Title
Bottom-Up Synthesis of Graphene Nanoribbons on Surfaces

Permalink
https://escholarship.org/uc/item/77x4x0ft

ISBN
978-3-319-64169-0

Author
Fischer, Felix R

Publication Date
2017

DOI
10.1007/12_2017_2

Peer reviewed

Bottom-Up Synthesis of Graphene Nanoribbons on Surfaces

Felix R. Fischer

Department of Chemistry, University of California Berkeley, Materials Sciences Division, Lawrence Berkeley National Laboratory and Kavli Energy Nanosciences Institute at the University of California Berkeley and Lawrence Berkeley National Laboratory, Berkeley, California 94720, United States of America

E-mail: ffischer@berkeley.edu

Abstract The review discusses the progress in the synthesis of atomically precise graphene nanoribbons from molecularly defined precursors on surfaces. It covers the literature from 2010 through 2016.

Keywords Graphene nanoribbon, bottom-up synthesis, surface catalysis, scanning tunneling microscopy/spectroscopy

Abbreviations

AFM	atomic force microscopy
AGNR	armchair graphene nanoribbon
CB	conduction band
CeGNR	cove edge graphene nanoribbon
CGNR	chevron graphene nanoribbon
DOS	density of states
GNR	graphene nanoribbon
HREELS	high-resolution electron energy loss spectroscopy
IPES	inverse photoemission spectroscopy
LDOS	local density of states
ncAFM	non-contact atomic force microscopy
STM	scanning tunneling microscopy
STS	scanning tunneling spectroscopy
UHV	ultra high vacuum
UPS	ultraviolet photoemission spectroscopy
VB	valence band
XPS	X-ray photoemission spectroscopy
ZGNR	zig-zag graphene nanoribbon

1 Introduction

The outstanding transformative potential of graphene, an infinite sheet of carbon atoms tightly packed into a honeycomb lattice, has been recognized mostly due to its exceptionally high charge-carrier mobility, thermal conductivity, tensile strength, and mechanical stiffness [1-3]. Yet, these undeniably very desirable properties represent only a very small facet of the true potential of all-sp^2 carbon materials and its potential to revolutionize the field of molecular electronics. The electronic properties of graphene itself can be described as a gapless semiconductor or semimetal (Figure 1) [4, 5]. Its valence and conductance band overlap in a single point. Graphene shows a strong ambipolar electric field effect. The charge carriers can be tuned continuously between holes and electrons reaching densities as high as 10^{13} cm^{-1} and mobilities in excess of 15000 $cm^2V^{-1}s^{-1}$. The charge mobility in graphene is largely dominated by impurity scattering effects and is almost independent of the temperature. Even at ambient conditions the charge carriers in graphene move ballistically over submicron distances covering a typical gap between the source and drain electrodes of a transistor in less than 1 ps [1, 2, 6].

Over the last decade an overwhelming variety of applications for graphene have been proposed ranging from fillers for composite plastic materials, graphene based batteries, super capacitors, and field emitters [7, 8], transparent electrodes in optoelectronics [9, 10], carbon-based environmental sensors [11], spin-valves [12, 13], and field-effect transistors [1]. The research in the field of all-sp^2 carbon-based materials has largely been motivated by its applications in advanced functional electronics. Due to its unique properties graphene has been identified as one for the most promising materials for post-silicon integrated circuit architectures [14]. The seamless integration of graphene into advanced electronic circuits, however, calls for semiconductors, rather than semimetals, featuring well-defined and tunable band gaps and large on-off current ratios at ambient conditions. This can be achieved by reducing the infinite two-dimensional carbon sheet to a narrow one-dimensional graphene nanoribbon (GNR) [5, 15]. This quantum mechanical confinement alters the electronic band structure and gives rise to a well-defined gap between the conductance and the valence band [16, 17]. In fact, GNRs most unusual properties, e.g. the theoretically predicted edge-magnetism, the exceptionally high spin-coherence, and the highly tunable band gap, are intimately linked to quantum mechanical boundary conditions dictated by the dimension, symmetry, and the edge-structure [18]. Unfortunately, these complex structure-function relationships remain poorly understood. The exploration, realization, and implementation of these truly exotic properties rely on the development of innovative synthetic strategies, that provide atomically precise control over the assembly of functional nanographene.

Superior synthetic strategies toward atomically defined and tunable GNRs must overcome several longstanding challenges. First and foremost is the reliable control of the absolute dimensions, i.e. length and width. Cutting-edge top-down lithographic patterning techniques have been successfully used to fabricate individual GNR featuring widths as narrow as 10 nm. The process however is exceedingly laborious, relies on the availability of sophisticated instrumentation, and is limited to the fabrication of individually unique samples. Synthetic bottom-up approaches instead have the potential to yield rationally designed GNRs in highly homogeneous batch synthesis. Structural variation of the small-molecule building blocks, the precursors for the GNRs, represents a reliable strategy to dial-in a desired width and edge symmetry. Pure samples of hydrogen terminated zig-zag (ZGNRs) or armchair GNRs (AGNRs) with homogeneous widths and highly reproducible physical properties can be obtained. Furthermore, this rational approach paves the way for the assembly of GNRs featuring designer-edges tailored to a variety of very specific application requirements. The extraordinary control over the structure of GNRs can also be applied to rational defect engineering or doping. The chemical synthesis of small-molecule precursors allows the introduction of functional groups or heteroatoms into the edges or into the carbon lattice of the GNR itself. The exact position of these dopants and the highly regular pattern along the length of the ribbons can easily be predicted and can be used to tune e.g. the Fermi energy, the band gap, or the number and the nature of charge carriers in the GNR.

2 Top-Down Synthetic Strategies

The controlled synthesis of GNR based functional materials is a field still in its infancy. The techniques used to synthesize GNRs can be broadly categorized into two complementary approaches: classical top-down patterning of two dimensional graphene sheets, and the controlled bottom-up growth of graphene nanostructures from small-molecule precursors. Early top-down approaches relied on lithographic techniques to pattern mechanically exfoliated sheets of graphene (Figure 2). Han et al. used e-beam lithography to pattern etch masks on single sheets of graphene [5]. Oxygen plasma etching of the unprotected graphene yielded individual GNRs with widths ranging from 10–100 nm and lengths of 1–2 μm. The electronic properties of these structures, however, suffer from harsh reaction conditions. Using this technique, it is difficult to control both the edge symmetry and the substitution pattern of the GNRs. Tapasztó et al. combined the surface modification and atomic resolution imaging capabilities of STM techniques to engineer graphene nanostructures [15]. Current etching of a single sheet of graphene at the surface of multilayer graphite yielded GNRs ranging in widths between 2.5–10 nm and lengths up to 120 nm. This technique represents a significant improvement, however, the low throughput and edge irregularities or roughness in the narrower ribbons remain a common problem of top-down approaches.

Naturally occurring defect structures in graphene have been used by Li et al. to fabricate sub 10 nm wide and ~ 1 μm long GNRs by sonication of exfoliated graphene sheets suspended in organic solvents [19]. While this approach yields GNRs with well-defined edges, the random distribution of defects can not be used to control the absolute dimensions of the ribbon. Kosynkin at al. and Jiao et al. have unzipped single-walled and multi-walled carbon nanotubes along the longitudinal axis to yield narrow graphene nanoribbons [17, 20, 21]. Both techniques rely on the use of exceptionally harsh reaction conditions, large excess of strong oxidants like $KMnO_4$ or plasma etching, to induce and propagate defects along the longitudinal axis of the nanotubes. The edge structure of the resulting unfolded GNRs can directly be correlated to the chirality of the initial carbon nanotube. The use of harsh reaction conditions and the inherent inhomogeneity of carbon nanotubes, however, lead to irregularities in the substitution pattern and unpredictable edge symmetries. Carbon atoms exposed during the unzipping process can easily be oxidized to e.g. alcohols, ketones, or carboxylic acids. This irregular substitution negatively and unpredictably affects the conductive properties of narrow GNRs.

3 Rational Bottom-Up Synthesis

A significant advance in the rational synthesis of GNRs has been demonstrated by Müllen, Fasel, and coworkers [22]. Pioneering work related to the surface supported assembly of molecular wires and covalent organic networks sparked the rational design of polymers that could be converted into GNRs through surface catalyzed cyclodehydogenation strategies [23-25]. The general concept is illustrated for the rational synthesis of N = 7 (where N is the integer number of carbon atoms counted across the width of the GNR) AGNRs from 10,10'-dibromo-9,9'-bianthryl (**1**) in Figure 3. The brominated small-molecule precursors is evaporated onto a clean noble metal (e.g. Au, Ag, Cu) surface held at a constant temperature (T_1) under ultra-high vacuum (UHV). The intimate interaction with the catalytically active metal surface induces the homolytic cleavage of the carbon–halogen bond to give a diradical intermediate. These intermediate carbon-centered diradicals diffuse along the surface and recombine in a step-growth polymerization to yield linear *poly*-anthracene chains. Thermal annealing of these precursors at an elevated temperature (T_2)

induces a cyclodehydrogenation sequence [26] that yields fully conjugated GNRs ranging in length from 12–60 nm [27]. This surface-based self-assembly technique yields 7-AGNRs with atomically defined hydrogen substituted armchair edges. The width and the crystallographic symmetry of bottom-up fabricated GNRs is primarily determined by the structure of the small-molecule precursor. The length of the ribbon largely depends on the surface coverage, the average diffusion length of monomers and growing polymer chains on the surface, and the competition between chain-extension, chain-termination and radical-transfer processes. While this technique yields superior GNRs with hydrogen terminated edges it is limited by the growth conditions. The efficient incorporation into devices demands GNRs with lengths in excess of 100 nm. Particularly for electronic applications it is essential that the GNR is supported by an insulator rather than by a highly conductive metal to prevent competing conduction pathways.

3.1 Bottom-Up Synthesis on Surfaces: Mechanism and Design Strategies

A central aspect to the rational bottom-up synthesis of GNRs lies in the design of the molecular precursors. The precursor molecules are required to meet a series of thermodynamic, kinetic, and structural criteria imposed by the dimensions and the symmetry of the desired GNR, the nature of the surface used as the growth substrate, and technical limitations imposed by the UHV system used in the fabrication. Figure 4 summarizes a selection of building blocks used in the synthesis of AGNRs, chevron GNRs (CGNRs), and ZGNRs on surfaces. Initial work has largely focused on the synthesis or AGNRs ranging in width from N = 5 to N = 13. A common structural feature of most molecular precursors is a mirror symmetry perpendicular to the long axis of the GNR. This preferred structure, an A–A building block, ensures that the rate of radical recombination at either end of the growing polymer chain is comparable. The inherent symmetry further circumvents structural defects that could emerge from asymmetric radical recombination of A–B building blocks featuring, for example, different steric demands at either end of the monomer. A second important structural consideration is the placement of aryl rings that undergo cyclodehydrogenation during the thermal annealing on the surface. As a post-polymerization step the successful defect free cyclodehydrogenation rests on a clear preference of the aryl rings to undergo exclusively the desired cyclization that leads to the extended conjugated π-system of GNRs. Careful structural considerations ensure that the appended aryl rings form the desired C–C bonds rather than participating in side reactions that could lead to kinks or defects along the GNR backbone. Conceptually this is illustrated in the design of the precursor for 13-AGNRs (Figure 5). The *ortho*-substitution of the bond between the biphenyl wing and the anthracene core gives access to only one distinct cyclodehydrogenation product as opposed to two potentially accessible orientations for the alternative *meta*-substitution pattern.

Further consideration has to be given to the choice of activating substituents. The large majority of successful building blocks feature either C–Br or C–I bonds that undergo homolytic cleavage to generate halogen radicals and the desired Csp^2 centered radicals that participate in the step growth polymerization. The preferential selection of Br and I substituents for the synthesis of GNRs on precious metal surfaces is not arbitrary but meets very specific kinetic and thermodynamic requirements. The key challenges are the choice of a functional group that is compatible with the sublimation conditions used during the deposition of molecular precursor on the target substrate, a bond that can be selectively activated through an external stimuli (e.g. heat, light) on the surface under conditions that do not cleave other labile bonds (C–H, C–C) in the molecule, and a homolytic fragmentation pattern that leaves a Csp^2 centered radical and preferably a small molecule behind that either irreversibly desorbs from the surface or is sufficiently deactivated to not interfere during the radical chain propagation step. These conditions are largely met in the activation of labile C–Br and C–I bonds over the omnipresent C–H bonds on Au, Ag and Cu surfaces. DFT calculations by Björk et al. have demonstrated that the highly exothermal bond dissociation of phenylbromide or phenyliodide (317 kJ mol^{-1} and 321 kJ mol^{-1} respectively) turns into an endothermal process on Au(111), Ag(111), and Cu(111) surfaces [28, 29]. This unusual thermodynamic stabilization can be explained by covalent interactions between the Csp^2 centered radical on the phenyl ring and the free valences of the metal surface. Chemisorption of the high energy phenyl radical drives the reaction towards the dissociated products. The ability for stabilizing the phenyl radical follows a trend in the series Au, Ag, Cu with the latter being the most reactive surface. Along with the overall reversion of the thermodynamic parameters, the kinetic barrier for the homolytic clavage of the C–Br or C–I bond follows a similar trend. The activation energy for the dissociation of the C–Br and C–I bonds is highest on Au (97 kJ mol^{-1} and 69 kJ mol^{-1}) and lowest on Cu (64 kJ mol^{-1} and 38 kJ mol^{-1}). These theoretical results are largely corroborated by experiments. Batra et. al and Simonov et al. followed the thermal activation of the C–Br bonds in **1** on a Au(111) surface using X-ray photoemission spectroscopy (XPS) [30, 31]. At temperatures below 100 °C the XPS of molecule decorated substrates indicates that **1** is only physisorbed on the surface (Figure 6). As the temperature is raised to 120–130 °C new signals for both C1s and Br3d appear that are consistent with the formation of a chemisorbed carbon and bromine radical. At 180 °C the reaction is complete and only the chemisorbed C and Br species can be observed. Further heating leads to the desorption of bromine (Br3d doublet at 68/69 eV disappears) while the carbon centered radical later undergoes recombination to form the polyanthracene precursor. Experimental data indicates that the radical step growth polymerization precedes the desorption of Br from the Au(111) surface by a few degrees [32]. The subtle difference between Br desorption and C–C bond formation energy is important, as omnipresent Br atoms on the surface can act as chain termination or radical transfer reagents during the step-growth polymerization phase. While Br and I groups are privileged motifs among molecular GNR precursors the structural scope is not limited to carbon–halogen bonds. Recent encouraging examples include thermally induced isomerization of enediynes that efficiently and regioselectively generate Csp^2 centered radicals that can recombine to form new C–C bonds [33, 34].

A more complex factor that has to be considered in the design of competent molecular precursors lies in the sample preparation procedure itself. Surface mediated GNR growth is commonly performed in a UHV system as the nature of the radical recombination that leads to the extended polymer precursors requires an atomically clean surface. The molecular building blocks for GNRs are commonly evaporated from a crucible onto the face of a single crystal of metal thin film. This step mandates a thermal stability that is compatible with the sublimation temperature, and preferably below the uncatalyzed activation of the thermally labile groups. Furthermore, an exceptionally high purity of the molecular sample is instrumental to the formation of extended polymers, as even trace impurities (< 0.1%) or decomposition products can readily sublime and form a monolayer coverage on the metal substrate before the desired building blocks can evaporate. Finally, even at 10^{-9} Pa, sublimation itself places an upper limit on the size of molecular precursors that can be deposited efficiently, and restricts the nature, the position, and the size of substituents that can be incorporated into the structure of the resulting GNR.

Even if all the above criteria are met through the rational design of a molecular building block, a series of less predictable factors remain. These include for example the preferred adsorption geometry and adsorption energy of the molecules on the substrate. Predicting the self-assembly of molecules on a surface solely based on routine DFT calculations in the gas phase is a daunting challenge and increases exponentially with any additional degree of freedom or decrease in symmetry inherent to the molecule itself. Aside from the numerous orientations a molecule can adopt with respect to the crystallographic axes and the unit cell of the underlying substrate, any non-planar molecule inherently has multiple surfaces that can adsorb to the substrate. When approaching monolayer coverages additional intermolecular interactions can induce the formation of long range ordered molecular islands. Since the step growth polymerization relies on a formal radical recombination, the physisorbed or chemisorbed intermediates have to come close enough to form a covalent C–C bond. During this critical step the relative orientation of reaction centers and the steric demand imposed by the immediate surrounding both contribute to the height of the activation barriers and thus the product distribution. This is illustrated in the fact that two molecules of the non-planar dibromobisanthrene **1** adsorbed on a Au(111) surface (dihedral angle between anthracenes ~ 80°) can approach one another in a staggered conformation that allows for the fusion of both radical centers. If instead a planar 9,10-dibromoanthracene were used the repulsive interaction between *peri*-hydrogens would effectively prevent the formation of a new C–C bond. As important as the relative orientation is a well-balanced molecule surface interaction. Adsorbates that interact too weakly with the substrate tend to form irregular clusters along crystallographic defects and step edges or desorb prematurely during the thermal activation steps. If instead the adsorption energy is too large the diffusion of activated species across the surface can become a rate limiting step. While molecular designs greatly benefit from structural analogies to proven systems, even in these cases the sheer complexity inherent to balancing the multitude of intermolecular forces along with the significant variability that comes with different metal substrates and crystallographic faces has thus far prevented the development of any practical predictive model. An illustrative example is the growth of GNRs form **1** on Au(111) vs Cu(111) (Figure 7). On Au(111) substrates **1** grows 7-AGNRs as expected based on the design considerations [22]. On the more active Cu(111) surface however the resulting GNRs feature a planar chiral (3,1) edge pattern resulting from the lateral fusion of molecular building blocks at an angle of 77° with respect to the intended axis of propagation [35-38].

The last and arguably more controllable step is the cyclodehydrogenation of the GNR polymer precursor on the metal substrate. If the molecular building blocks have been carefully designed every aryl ring can only fuse in one unique and predictable position. Extensive DFT calculations based on the cyclization of a 9,9’-bianthracene model on Au(111) performed by Björk et al. demonstrate that the precious metal surface plays a key role in the cyclodehydrogenation step [26]. While a number of plausible stepwise processes were considered the lowest activation barrier is associated with a concerted mechanism that sees the aryl rings rotate towards one another to form a new C–C bond while the *ipso* H-atoms at the corresponding positions are transferred to the Au(111) substrate as atomically chemisorbed hydrogen. The metal substrate thus acts as a catalyst that facilitates the dissociation of H-atoms. An additional cooperative effect has been observed in the study of extended *oligo*-anthracene model systems. The planarization and the strain induced by a first random cyclodehydrogenation drastically decreases the activation barrier for the cyclization of immediately adjacent rings. On Au(111) surface the cyclodehydrogenation proceeds in a cascade emanating in both directions from an initial arbitrary starting point. While this special case of positive cooperativity is rather unique to the synthesis of

7-AGNRs form **1** and related structures, the lowering of the activation barrier for adjacent cyclizations induced by the distortion imparted by the initial C–C bond formation is a commonly observed phenomenon in surface catalysis with on Au, Ag, and Cu.

3.2 Rationally Tuning the Energy Structure in Bottom-Up Fabricated GNRs

Quantum mechanical calculations have proven to be a valuable tool to predict the band structure of functional organic materials. A variety of theoretical models e.g. tight binding, density functional theory, and *GW* approximations that include the self-energy of a many-body system of electrons, have been applied to GNRs reflecting varying levels of accuracy [39, 40]. While the absolute numbers reflecting e.g. the magnitude of the band gap, the density of states of the energy of the valence (VB) and the conductance band (CB) edges diverge significantly between various theoretical models the underlying general trends are consistent throughout a family of structurally related GNRs. For consistency and to avoid confusions we will herein refer to calculations based on the *GW* approximation wherever possible.

Hydrogen terminated GNRs featuring an armchair pattern along the edges are predicted to be intrinsic semiconductors. The magnitude of the band gap between the valence and the conductance band edges roughly scales inversely width of the GNR (Figure 8) [40]. This general trend is consistent within all three families of armchair GNRs: the width is expressed as the number of atoms N = 3p, N = 3p+1, and N = 3p+2 counted in a straight chain across a ribbon (p = 0, 1, 2, 3, ...). The smallest band gaps have been predicted for the 3p+2 series, whereas the largest band gaps are expected for members of the 3p+1 family. The width dependence of semiconducting AGNRs allows to rationally dial-in a desired band structure by tightly controlling the structure of the molecular precursor. Experimental determination of the band gaps in a family of AGNRs adsorbed on Au(111) supports this general trends. The quasi-particle band gaps of 7-AGNRs, 9-AGNRs, and 13-AGNRs determined by scanning tunneling spectroscopy (STS) are 2.3 eV, 1.4 eV and 1.4 eV respectively. While 7-AGNRs and 13-AGNRs, derived from **1** and **2** respectively, belong to the same family (3p+1) and serve to illustrate the reduction in band gap for wider ribbons, 9-AGNRs derived from **3** fall into the intermediate 3p series and only coincidentally feature a band gap that is comparable to the significantly wider 13-AGNRs. Figure 9 depicts and overlay of d*I*/d*V* spectra of 7-AGNRs and 13-AGNRs recorded on a Au(111) crystal [41]. The smaller intrinsic band gap of 13-AGNR (blue), corresponding to a peak to peak distance in a density of states plot, is straddled by the significantly larger gap of the 7-AGNRs (red). It is worth noting that theoretical models based on the DFT *GW* approximation do generally not include a discrete interaction between the GNRs and the underlying metal substrate. A direct comparison between the calculated quasi-particle band gap of isolated GNRs (3.8 eV, 2.0 eV and 2.4 eV for 7-AGNRs, 9-AGNRs and 13-AGNRs, respectively) and the experimentally determined band gaps is thus restricted by limitations in the accuracy of the models describing the hybridization of the GNR with the surface states. Zhang et al. and Kimouche et al. have expanded the series of AGNRs to include a member of the 3p+2 family associated with the smallest theoretically predicted band gaps. Both tetrabromonaphthalene **4** and the isomeric dibromoperylenes **5** serve as molecular precursors for 5-AGNRs [42, 43]. While initial STS on Au(111) appeared to indicate an unusually large bandgap (2.8 eV) a careful study of a series of oligomers derived from 5-AGNRs ranging in length between 2 to 14 monomer units (**5**) revealed a more detailed picture. Aside from the dominant signals previously assigned to the CB and VB edges the study revealed a series of smaller peaks in the d*I*/d*V* spectrum that fall within the assumed band gap (Figure 10). Reassignment of the CB and VB states led to a reinterpretation of the DOS and revealed an exceptionally small band gap of 0.1 eV for ribbons featuring more than five monomer units [43]. This lower band gap is consistent with the expected trend for the 3p+2 family (1.7 eV for 7-AGNRs)

Aside from varying the width of GNRs the unique structural control inherent to a rational bottom-up synthesis offers a variety of alternative strategies to tailor the electronic structure. CGNRs derived from the dibromotriphenylene precursor **6** for example can be thought of as a GNR comprised of hexabenzocoronenes laterally fused at an angle of (~104°) [22]. STS on Au(111) reveals an intermediate band gap of 2.0 eV [44]. For comparison, the theoretically predicted band gap calculated using the *GW* approximation is 3.5 eV. Optical spectroscopy of identical CGNRs shows a still unresolved departure from these values. High-resolution electron energy loss spectroscopy (HREELS) and ultraviolet photoemission/inverse photoemission spectroscopy (UPS/IPES) show band gaps of 2.8 eV and 1.3 eV respectively [45, 46]. A resolution of this apparent contradiction is pending further detailed investigation.

Liu et al. introduced a class of planar chiral GNRs derived from dibromobischrysene **7** [47]. The structure of these cove-edge GNRs (CeGNRs) resembles a zig-zag edge in which every fourth carbon atom has been replaced by hydrogen. Deposition of **7** on Au(111) followed by thermal annealing and cyclodehydrogenation yields GNRs ranging in length between 5–20 nm. The unique edge structure of these chiral GNRs however is unusually susceptible to unselective C–H activation. Concurrent hydrogen abstraction during the cyclodehydrogenation step leads to ubiquitous radical centers along the edges that undergo recombination or uncontrolled radical transfer processes. As a result of this insufficient selectivity, CeGNRs tend to fuse into larger irregular GNR aggregates at temperatures commensurate with the cyclodehydrogenation step. Optical spectroscopy along with ab initio DFT calculations (not including the *GW* approximation) indicate a potentially small band gap of 1.7–1.9 eV.

Narrow ZGNRs featuring a zig-zag pattern of hydrogen terminated carbon atoms along the longitudinal edge feature a series of unique properties among bottom-up fabricated GNRs. Theoretical calculations predict that the edge states are ferromagnetically coupled along one zig-zag edge and antiferromagentially with respect to the other edge. These spin polarized electronic states are of great interest for advanced functional materials for spintronics. Ruffieux et al. demonstrated the bottom-up synthesis of N = 6 ZGNRs (where N is the number of carbon zig-zag chains counted across the width of the ribbon) form the unusual molecular precursor **8** (Figure 11) [48]. While all AGNRs and CGNRs feature a long axis that is aligned parallel to the armchair edge, the long axis in ZGNRs is perpendicular to the preferred growth direction of halogen-based surface polymerizations. The anchor shaped design of molecular precursor **8** elegantly resolves this challenge by arranging in an alternating head-to-toe orientation that aligns the long axis of the GNR with the zig-zag edge while retaining the preferred relative orientation of the new C–C bond formed during the radical step growth polymerization. Lastly the two additional methyl groups were incorporated into the structure of **8** to close the remaining gaps along the zig-zag edges of 6-ZGNRs. STS of 6-ZGNRs that have been transferred from the Au(111) gold substrate onto an insulating NaCl layer show a band gap of 1.5 eV. As the 6-ZGNR is mechanically decoupled from the interaction with the Au surface states the experimental values superbly match the theoretically predicted band gap (1.4 eV) calculated using the single particle Green's function and a screened Coulomb interaction (*GW* approximation). Further investigation of the exotic electronic and magnetic properties of ZGNRs along with a redoubled effort to stabilize the chemically reactive zig-zag edges is ongoing and holds great promise for the development of graphene based spintronic devices.

3.3 Substitutional Doping in Bottom-Up fabricated GNRs

While the extraordinary structural control innate to a rational bottom-up synthesis of functional graphene nanomaterials is superior to classical inorganic semiconductors, the rising complexity of structure-function relationships are at present a critical limitation to a robust performance-driven materials design. Instrumental tools and strategies to tailor the band structure and the Fermi level of GNRs require a deeper understanding of how atomistic structure guides the alignment of energy states. In particular, the concept of doping in atomically defined nanoscale graphene structures extends beyond the bounds of classical theories derived for inorganic semiconductors and has been the topic of extensive exploration. Theoretical models predict that the energy of the VB and CB of semiconducting GNRs can be tuned by introducing a highly regular pattern of electron donating or electron withdrawing functional groups or atoms along the edges of GNRs (Figure 12). Early on this edge-doping has been at the center of investigation as it represents the least intrusive chemical modification that can readily be incorporated into the structure of molecular precursors. Bronner et al., Cai et al., and Vo et al. demonstrated that the introduction of nitrogen atoms in the form of pyrimidine and pyridine rings into the edges of CGNRs induces a rigid band shift (Figure 13) [44, 45, 49]. Theoretical calculations indicate the magnitude of the band gap shift correlates with the number and only to a lesser extent with the position of the heteroatoms. Electronic HREELS spectra of CGNRs derived from **6** (0 N-atoms), **9** (1 N-atom), and **10** (2 N-atoms) reveal that the overall magnitude of the band gap remains largely unchanged (2.8 eV, 2.8 eV, and 2.7 eV respectively). UPS spectroscopy shows a rigid shift of the entire band structure to lower energy with increasing number of N-atoms (~0.1 eV per N-atom). STS of CGNRs grown on Au(111) from dipyrimidine precursor **11** (4 N-atoms) show a band gap of 2.0 eV that is comparable to the parent unsubstituted CGNRs. Yet, both VB and CB of CGNRs derived from **11** are shifted by 1.1 eV to lower energy. This general trend is supported by DFT calculations and extends the series of nitrogen edge-doping patterns in CGNRs up to 8 N-atoms. Based on theory an average shift of ~0.13 eV can be attributed to each N-atom. Computationally this concept has been applied to the introduction of boron atoms along the edges of CGNRs. As expected the direction of the rigid band shift is inverted (toward higher energy) while the magnitude amounts only to ~0.06 eV per boron atom.

Examples of edge doping are not restricted to the family of CGNR. Nguyen et al. demonstrated that a similar concept can not only be applied to the structurally more diverse family of AGNRs, but can also be extended to include group VI elements [50]. The molecular precursors for sulfur doped AGNRs (**12**) were derived from the structure of **2** by replacing one phenyl ring on each side by a thiophene. Even though the Pauling electronegativity of S-atoms is only marginally different from C-atoms (2.55 vs. 2.58), the hybridization of the heteroatom lone-pair with the conjugated π-system enhances the energy splitting between the CB (VB) and CB+1 (VB–1), respectively (Figure 14). The reorganization of the energy band structure leads to an overall reduction of the intrinsic band gap when compared to the parent 13-AGNRs. A notable distinction between nitrogen-doping in CGNRs and sulfur-doping in AGNRs is the overlap of the filled lone pair on sulfur (p-symmetry) with the p-orbitals on carbon that form the backbone of the GNR. The nitrogen lone pair in CGNRs instead is orthogonal and cannot interact directly with the GNR π-system. This previously unappreciated distinction opens entirely new avenues to tailor the density of states proximal to the band edges, a feature particularly relevant to tuning optical transitions in GNRs.

An indispensable technology required for the development of GNR based electronic devices is the ability to tune the local charge carrier density by introducing shallow donor (n-type) and acceptor states (p-type) proximal to the CB and VB edges, respectively. Edge-doping, as outlined above, however, only shifts the energy of band edges without introducing dopant states within the band gap. Substitutional n-/p-doping, that is, the introduction of filled/empty donor or acceptor states into the intrinsic gap of atomically defined GNRs, instead requires the incorporation of dopant heteroatoms at deterministic positions preferably along the backbone of the ribbon where the filled/empty p-orbitals are forced into conjugation with the extended π-system. Cloke et al. and Kawai et al. were the first to demonstrate rational backbone doping in AGNRs by using 5,10-bis(10-bromoanthracene-9-yl)-5,10-dihydroboranthrene (**13**) as a molecular precursor for N = 7 AGNRs [51, 52]. Non-contact atomic force microscopy (ncAFM) with carbon monoxide functionalized tips reveals a characteristic pattern of anthracene/boranthrene/anthracene units along the backbone of the GNR. In figure 15 the contrast at the position of the boron atoms appears darker due to the strong interaction of the empty p-orbitals with the surface states of the underlying metal. First-principles calculations based on the *GW* approximation including the screening effects from the underlying Au(111) substrate show a new empty state in the middle of the band gap of 7-AGNRs. The DOS of both the VB and this new CB bands show significant contributions (~10%) from B-atoms. Substitutional boron-doping along the backbone of 7-AGNRs thus introduces a deep lying acceptor band approximately 0.9 eV above the VB maximum. The theoretically predicted quasiparticle band gap is significantly smaller than that for the undoped pristine 7-AGNRs (~2.1 eV) calculated at same level of theory. The interpretation of dI/dV of boron-doped 7-AGNRs on Au(111) is challenging as the peak corresponding to the VB coincides with the surface states of the Au(111) substrate. A clearer signal can be obtained for the CB and CB+1 states at 1.0 eV and 1.6 eV. Better results have recently been obtained by growing boron-doped 7-AGNRs on Ag(111) surfaces. The surface state of Ag(111) is shifted with respect to Au(111) and allows for the unambiguous identification of all four VB–1 (–1.0 eV), VB (–0.3 eV), CB (1.1 eV), and CB+1 (1.5 eV) states for boron-doped 7-AGNRs. As expected the experimental band gap ~1.4 eV is significantly smaller than the corresponding gap of pristine 7-AGNRs (2.3 eV).

3.4 Spatial Isolation of Energy States in Segmented GNRs

Rectification, resonant tunneling, and light harvesting are just a few examples of dynamic processes that are intimately linked to the transport of charge carriers across a boundary between materials with dissimilar energy band structures. While harnessing the corresponding performance in a single GNRs holds great promise for further device miniaturization and superior energy efficiency, the microscopic structure and the underlying physics of energy band alignment at intraribbon heterojunction interfaces is still a topic of intense investigation. The unique control inherent to the rational bottom-up synthesis along with high resolution imaging (STM, ncAFM) and spectroscopic (STS) tools provide a path to a deterministic design of single GNR functional heterostructures devices. While the preparation of segmented polymers through traditional solution based methods is well established in the literature the surface facilitated synthesis described herein imposes a series of new challenges. The design of segmented GNRs featuring e.g. two distinctive molecular precursors, two different band structures, or two unique doping patterns requires that both building blocks A and B are structurally compatible. This requirement guarantees that the cyclodehydrogenation at the interface between to segments proceeds efficiently and the resulting heterojunctions are atomically defined. The second, arguably more challenging problem, is the development of new synthetic strategies that provide control over the sequence and the segmentation in GNR heterostructures. As discussed in section 3.1 the step-growth polymerization of activated molecular building blocks on a precious metal surface relies formally on a radical recombination mechanism. The sequence at which monomers are incorporated into the growing polymer chain is largely random and current strategies lack the exquisite control developed for block-copolymer synthesis in solution.

Cai et al. demonstrated the assembly of CGNR heterojunctions formed from molecular building blocks **6** and **11** [53]. Alternating evaporation both precursors onto a Au(111) surface held at 200 °C followed by standard cyclodehydrogenation leads to CGNRs featuring an alternating pattern of segments composed of **6** and **11**. While a sequential deposition offers a rudimentary control over the concentration of activated building blocks on the surface the random nature and the unfavorable kinetics of the step growth process do not provide GNRs with a reproducible sequence of heterojunctions. While CGNR segments formed from **6** and **11** are structurally almost indistinguishable by topographic STM the difference in their composition becomes apparent in STS mapping (Figure 16). dI/dV maps recorded at –0.35 V and –1.65 V show a distinctive alternating contrast characteristic for the VB of CGNRs formed from **6** and **11** respectively. The band gap in the nitrogen edge-doped segments is rigidly shifted to lower energy with respect to the undoped CGNRs. DFT calculations (Figure 17) reveal that the electronic structure of a seamlessly fused **6**/**11** CGNR interface resembles a staggered gap type II heterojunction. Both the VB and the CB are offset by 0.45 eV and 0.55 eV respectively. The band bending at the interface is exceptionally sharp. The band respective band structures reach essentially bulk properties within only 2nm from the interface. The significant electrostatic potential across the **6**/**11** CGNR heterojunction has promising implications for the device applications that require an efficient charge separation such as GNR based photovoltaics.

Chen et al. successfully assembled intraribbon heterojunctions comprised of fused segments of 7- and 13 AGNRs [54]. Co-deposition of molecular precursors **1** and **3** onto a Au(111) surface held at 24 °C followed by stepwise annealing at 200 °C and 400 °C leads to extended AGNRs featuring alternating widths (Figure 18). The narrower segments (~1.3 nm) are comprised of 7-AGNRs while the wider segments (~1.9 nm) correspond to 13-AGNRs. d*I*/d*V* spectra recorded at the highlighted positions above the respective GNR segments reflect the expected band structure for 7- and 13-AGNRs; a large band gap (2.7 eV) for the 7-AGNR segment and a small band gap (1.5 eV) for the 13-AGNR segment respectively. The respective band structures are highly localized in their respective segments and do not significantly extend beyond the heterojunction. If the STM tip is placed immediately above a 7-13 junction two additional highly localized states (1.25 V and 1.15 V) can be observed in the d*I*/d*V* spectrum. These states are unique to the interface and lie just below the CB of the 13-AGNRs. The relative band alignment is reminiscent of a straddling gap type I semiconductor junction. The lowest unoccupied (highest occupied) state in the N = 13 segment is lower (higher) than that in the N = 7 segment. In this unique band arrangement, a 7-13-7-AGNR sequence can be thought of as a quantum well for charge carriers trapped in the 13-AGNR segment. This architecture provides opportunities for designing graphene quantum-dot devices with sub nanometer feature size.

While the above examples highlighted the functional complexity that can be integrated into a single GNR, the limited control over the length and the sequence of individual segments within bottom-up fabricated GNR remains a grand challenge in the field. An alternative to the sequential co-deposition strategy outlined above has been proposed by Blankenburg et al. [55]. They noticed that the cyclodehydrogenation of *poly*-anthracene, the intermediate resulting from the radical polymerization of **1** on Au(111) surfaces, can be stopped at an intermediate stage. As the cyclodehydrogenation proceeds through a cooperative mechanism (see section 3.1) along the backbone of the GNR, the reaction can be stopped at a stage where segments of fully cyclized and partially cyclized 7-AGNRs coexist within the same ribbon. STM images of 7-AGNRs featuring partially cyclized 5^+-AGNR segments are depicted in figure 19. While this method formally yields GRN heterojunctions, there is no control over the sequence or the position of the junction within the ribbon. If the cyclodehydrogenation is induced by STM tip pulsing, segments of partially cyclized 5^+-AGNR could selectively be converted into 7-AGNRs. While STM tip manipulation of individual GNRs certainly is not a viable strategy for bulk fabrication the use of a secondary patterning step would overcome the challenges inherent to the uncontrolled step growth polymerization.

Marangoni et al. demonstrated an alternative edge-doping strategy toward segmented CGNRs that relies on a late stage interconversion of a reactive functional group.[56] Rather than relying on the co-polymerization of two dissimilar molecular precursors, the structure of dibromotriphenylene **14** incorporates a 9-methyl-9*H*-carbazole substituent as an internal reactive moiety along the convex protrusions of CGNR. Thermal activation of 9-methyl-9*H*-carbazole interconverts the functional group into either an electron rich carbazole, by cleavage of the N–CH_3 bond, or an electron deficient phenanthridine group, through a radical ring expansion mechanism. ncAFM images (Figure 20) clearly show the segmented structure in CGNRs featuring either five membered or six membered rings along the edges of the GNR. Late stage functionalization strategies hold great promise in the context of rational GNR heterostructure engineering as they potentially allow the site specific doping of prefabricated GNRs through a secondary activation step, e.g. light, heat, current.

4 Conclusion

The rational bottom-up synthesis of GNRs on solid supports has been instrumental in developing the fundamental understanding of the exotic physical properties emerging from lateral quantum confinement effects in graphene nanostructures. The unique insight gained from width modulation, edge-doping, backbone doping and the deterministic design of intraribbon GNR heterojunctions has demonstrated the potential and inspired new perspectives for their implementation in future generations of electronic devices. An implication of these visionary concepts still faces a multitude of technical challenges that require a coordinated interdisciplinary approach including the development of novel synthetic tools and techniques associated with the chemistry of molecular precursors, the exploration of the reactivity and the physical processes governing the self-assembly on surfaces, the access to high resolution and high throughput physical characterization techniques, and ultimately the integration with current electronic circuit architectures.

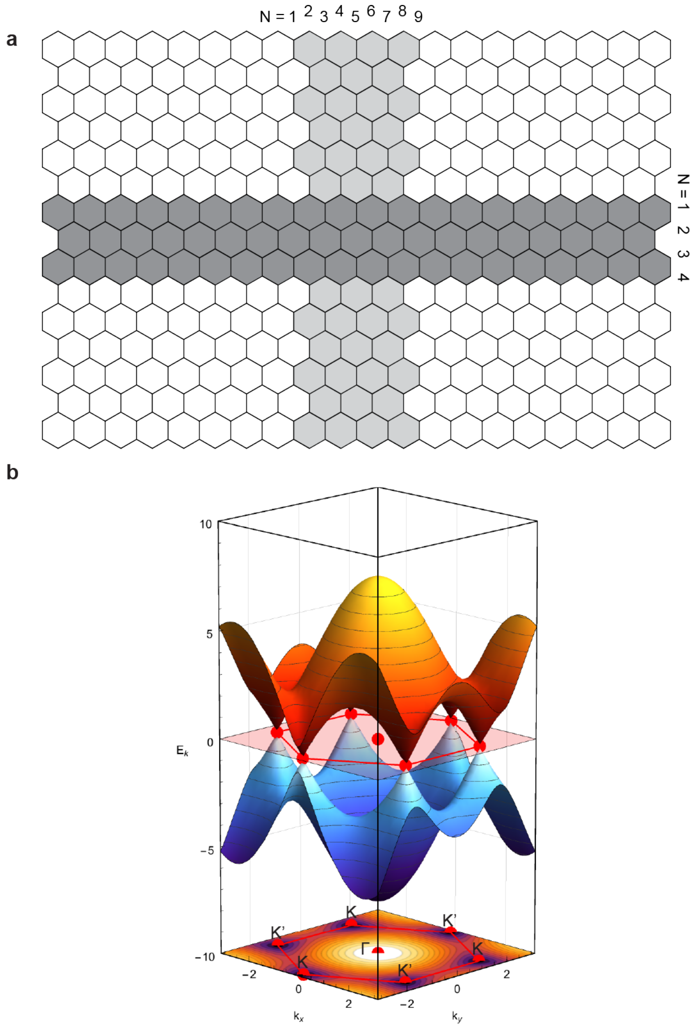

Figure 1 a) Schematic representation of graphene and graphene nanoribbons with armchair edges (vertical) and zig-zag edges (horizontal). The numbering used to define the width of the armchair GNRs (AGNRs) and zig-zag GNRs (ZGNRs) is denoted along the edges. b) Schematic representation of the electronic band structure in graphene featuring a linear dispersion at the Dirac points K and K’.

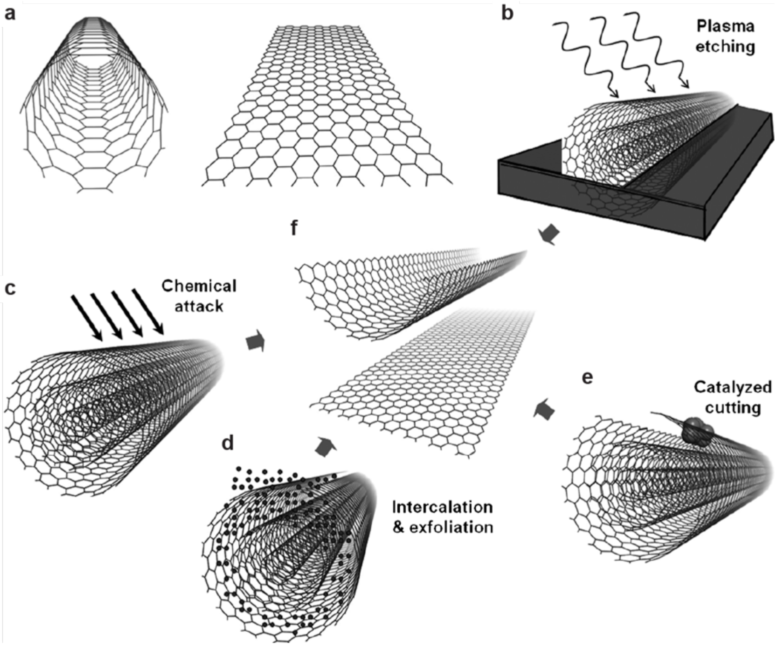

Figure 2. a) single walled carbon nanotubes (SWCNT) and graphene nanoribbon (GNR). Top-down synthetic approaches toward GNRs: b) plasma etching [20], c) longitudinal unzipping through chemical attack [17], d) intercalation of alkali metals followed by exfoliation of CNTs [57], e) metal nanoparticle catalyzed unzipping of CNTs [58], f) unfolded GNRs. Reproduced with permission from ref. [59], Copyright (2012) John Wiley and Sons.

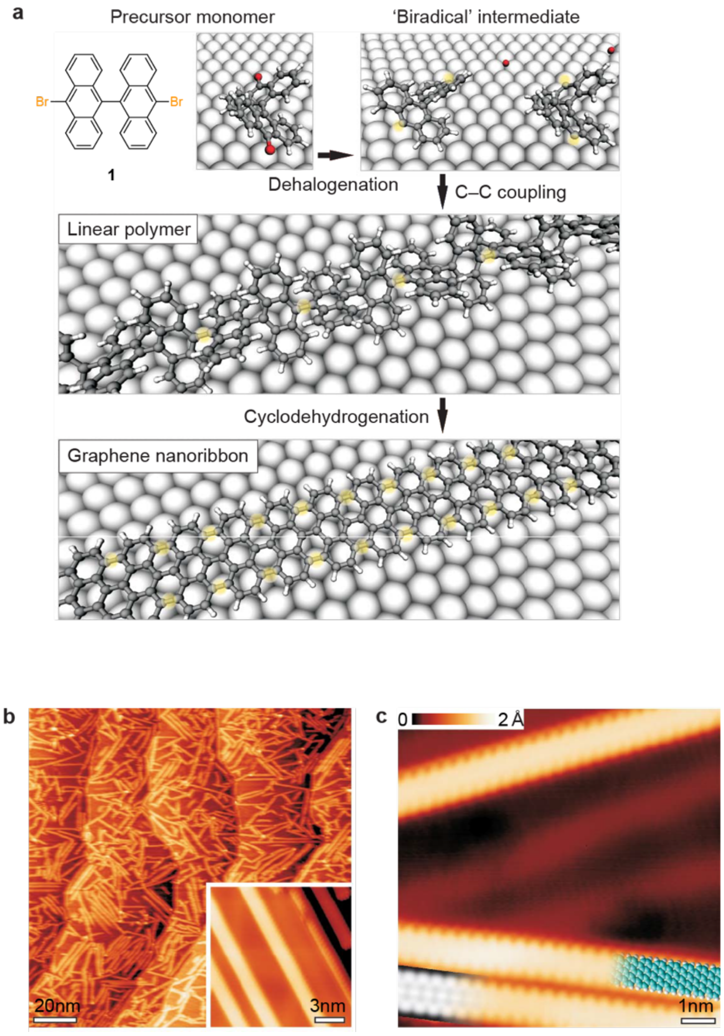

Figure 3. a) General scheme for the stepwise bottom-up synthesis of GNRs on Au(111). Key steps are the activation of the monomer precursor through dehalogenation, recombination to form a new C–C bonds, and cyclodehydrogenation to form fully extended 7-AGNRs. b) Large area STM image og 7-AGNRs on Au(111). c) magnified image of 7-AGNRs showing the smoothe hydrogen terminated armchair edges. A CPK model of 7-AGNR nanoribbons is overlaid as a guide to the eye. Reproduced with permission from ref. [22], Copyright (2010) Nature Publishing Group.

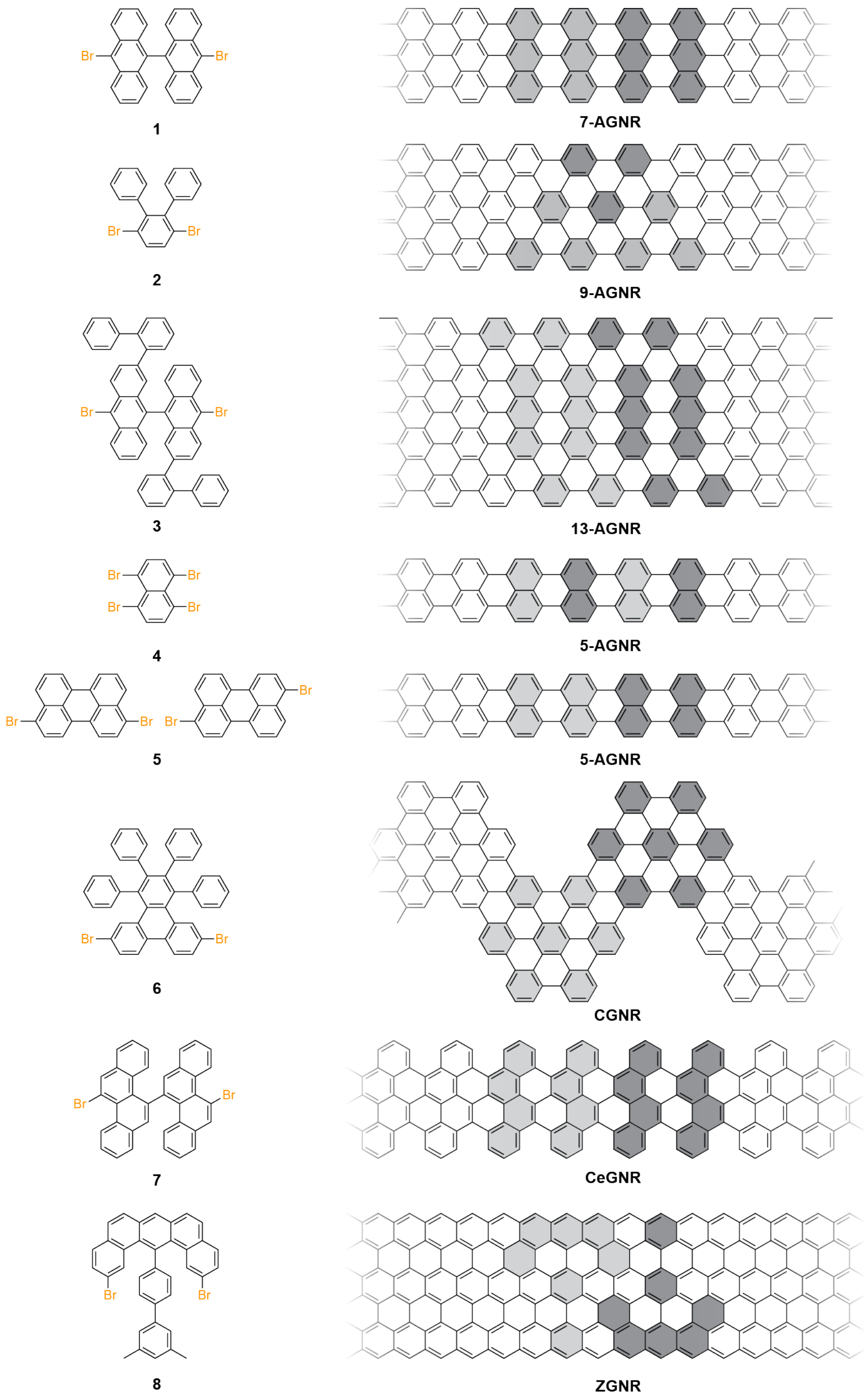

Figure 4. Schematic representation of AGNRs [22, 41-43], CGNRs [22], CeGNRs [47], ZGNRs [48] and the respective molecular precursors used in their synthesis on Au, Ag, or Cu surfaces.

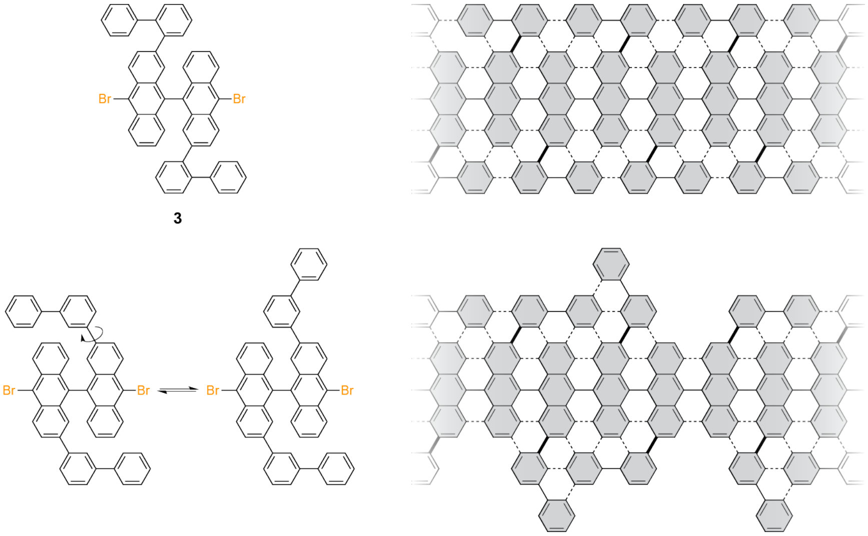

3

Figure 5. Two possible designs for 13-AGNR precursors. Only precursor **3** is set up to exclusively cyclize to form the desired defect free armchair edge. Rotation around the anthracene biphenyl C–C bond in the *meta* substituted precursor can lead to two possible cyclodehydrogenation patterns.

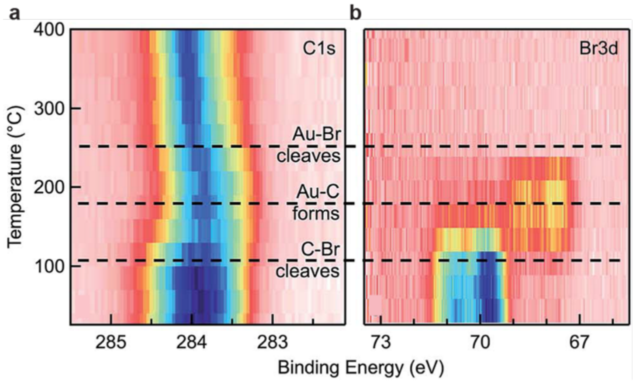

Figure 6. Temperature dependent XPS for a) C1s and b) Br3d for **1** on Au(111). The three dashed lines correspond to the onset of the homolytic C–Br cleavage, the surface stabilized radical intermediates, and the desorption of Br from Au(111). Reproduced with permission from ref. [30], Copyright (2014) Royal Society of Chemistry.

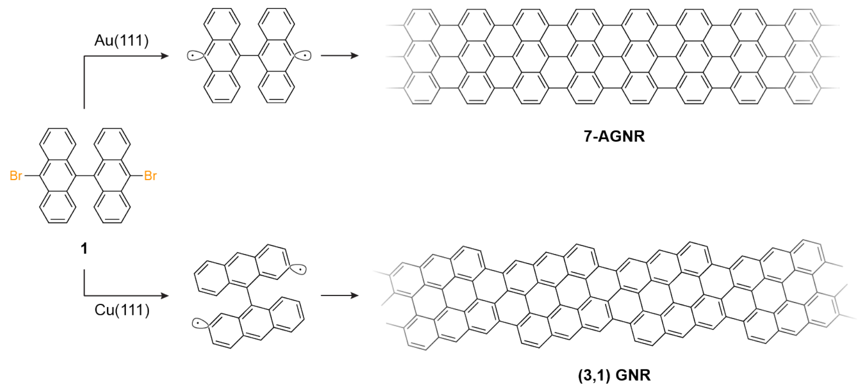

582 **Figure 7.** 7-AGNR and chiral GRNs featuring a (3,1) edge pattern formed from the same precursor **1** on Au(111) and Cu(111) surfaces respectively[35-37].

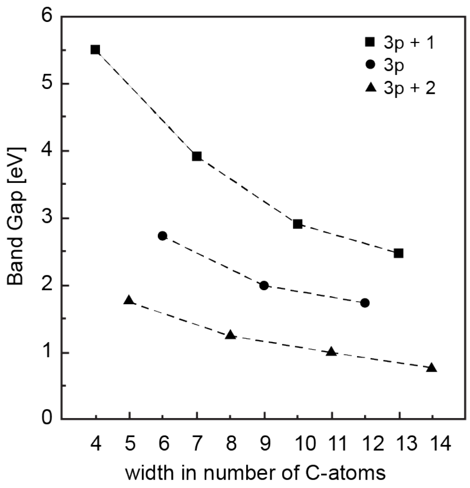

Figure 8. Correlation of *GW* band gaps with the number of carbon atoms across the width of AGNRs. The three families of AGNRs are represented by filled squares (3p+1), circles (3p), and triangles (3p+2). AGNRs belonging to the same family are connected by dotted lines as a guide to the eye. [40]

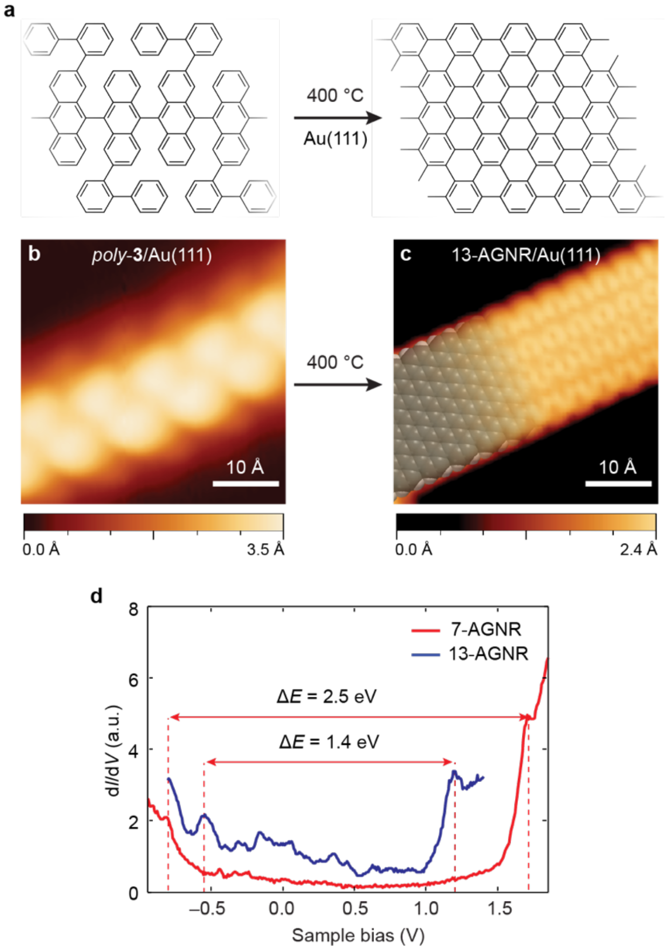

Figure 9. a) Schematic representation of the synthesis of 13-AGNRs from **3**. At 400 °C a cyclodehydrogenation sequence converts *poly*-**3** into 13-AGNRs. b) STM image of the *poly*-**3**. The polymers are nonplanar with an apparent height of 3.5 Å. c) STM image of 13-AGNRs formed after annealing poly-3 at 400 °C. A CPK model of a 13-AGNR has been overlaid onto the STM image as a guide to the eye. d) d*I*/d*V* spectra of 13-AGNR (blue) and 7-AGNR (red) on Au(111). Adapted with permission from ref. [41], Copyright (2013) American Chemical Society.

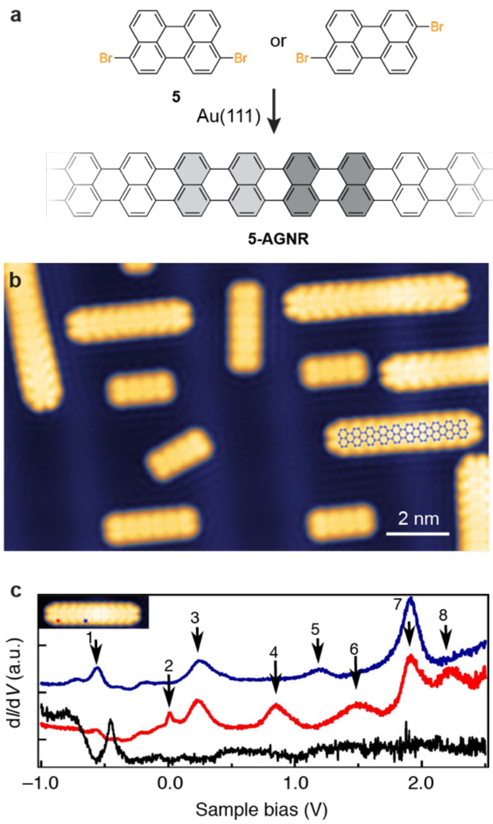

Figure 10. a) Schematic representation of the synthesis of 5-AGNRs from **5**. b) STM image of 5-AGNRs on Au(111). c) d*I*/d*V* spectra acquired on five monomer 5-AGNR are the positions (red and blue star) marked in the STM inset. Reproduced from ref. [43].

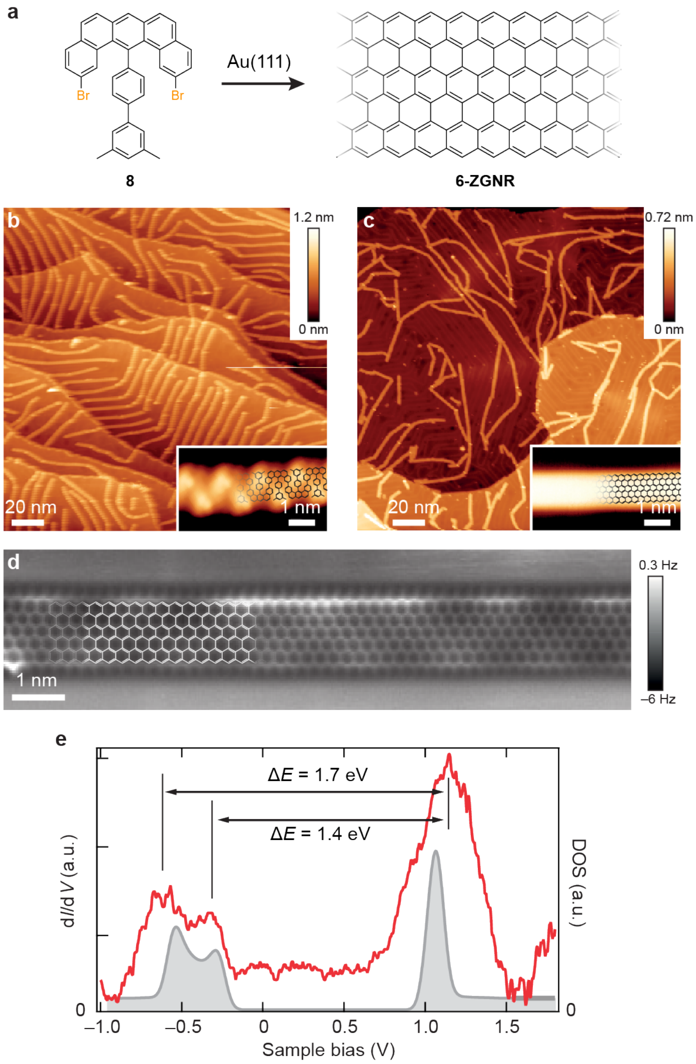

Figure 11. a) Schematic representation of the synthesis of 6-ZGNRs from **8**. b-c) Large area STM image of *poly*-**8** and 6-ZGNRs on Au(111). d) ncAFM of 6-ZGNRs showing the hydrogen terminated zig-zag edge. e) d*I*/d*V* spectrum (red) recorded at the zig-zag edge of a 6-ZGNR partially suspended on a NaCl monolayer island on Au(111) and calculated DOS (gray). Reproduced with permission from ref. [48], Copyright (2016) Nature Publishing Group.

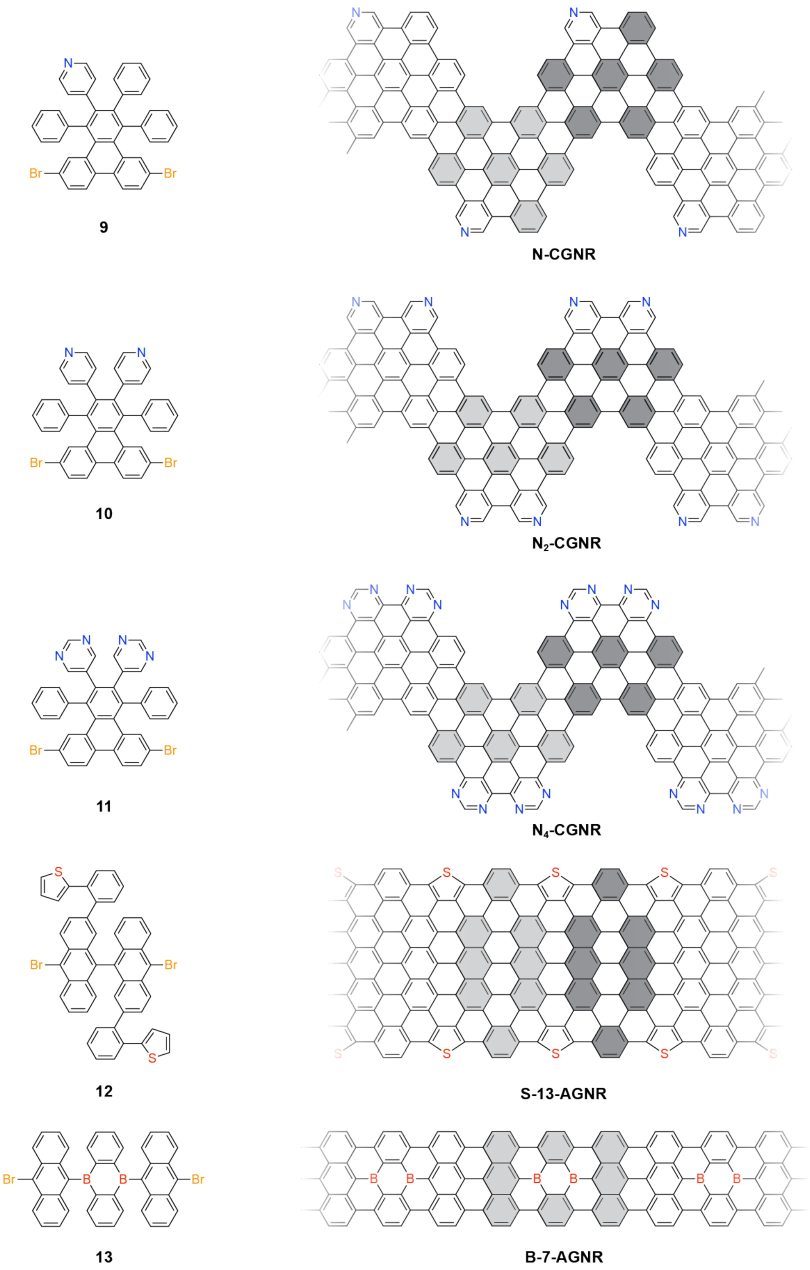

Figure 12. Schematic representation of examples for nitrogen edge-doping in CGNRs [44, 45, 49], sulfur edge-doping in 13-AGNRs [50], and backbone boron doping in 7-AGNRs [51, 52].

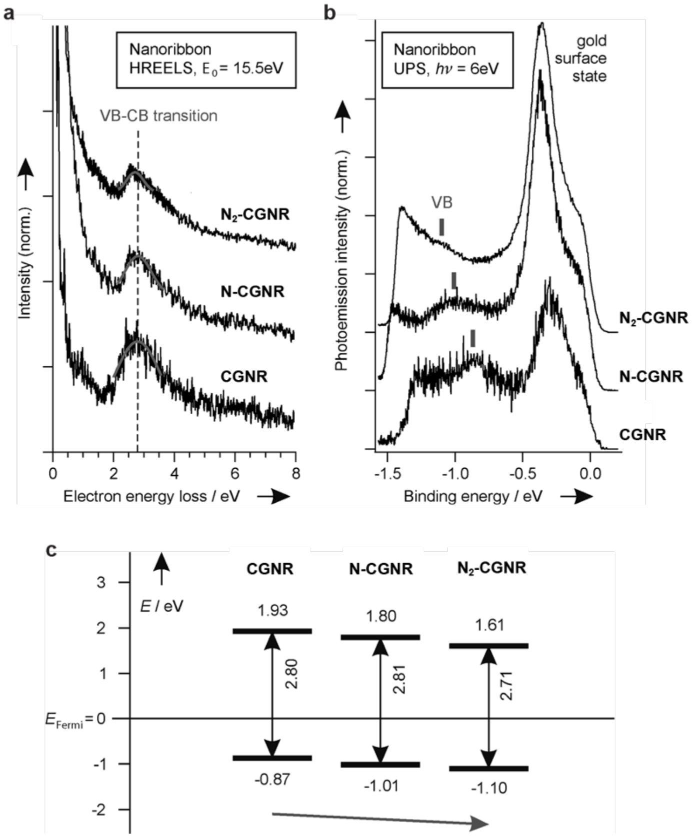

Figure 13. a) Electronic HREELS spectra for CGNRs edge doped with zero, one and two nitrogen atoms. The VB–CB transition is essentially unperturbed by the doping. b) UPS spectra of CGNRs, N-CGNRs, and N_2-CGNRs on Au showing the shift in the VB edge towards lower energy. c) Summary of the band gap, VB and CB alignment derived from HREELS and UPS spectroscopy. Reproduced with permission from ref. [45], Copyright (2013) John Wiley and Sons.

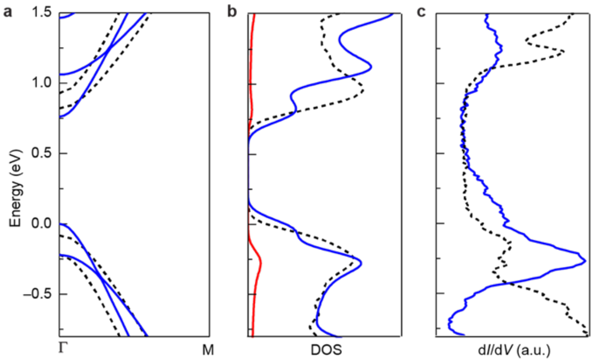

Figure 14. Calculated band structure of a) S-13-AGNR (blue) and undoped 13-AGNR (black). b) Calculated DOS of a S-13-AGNR (blue), the partial density of states (PDOS) of sulfur orbitals (red), and the DOS of a undoped 13-AGNR (black). c) Experimental d*I*/d*V* spectrum for S-13-AGNR (blue) and undoped 13-AGNR (black). Reproduced with permission from ref. [50], Copyright (2016) American Chemical Society.

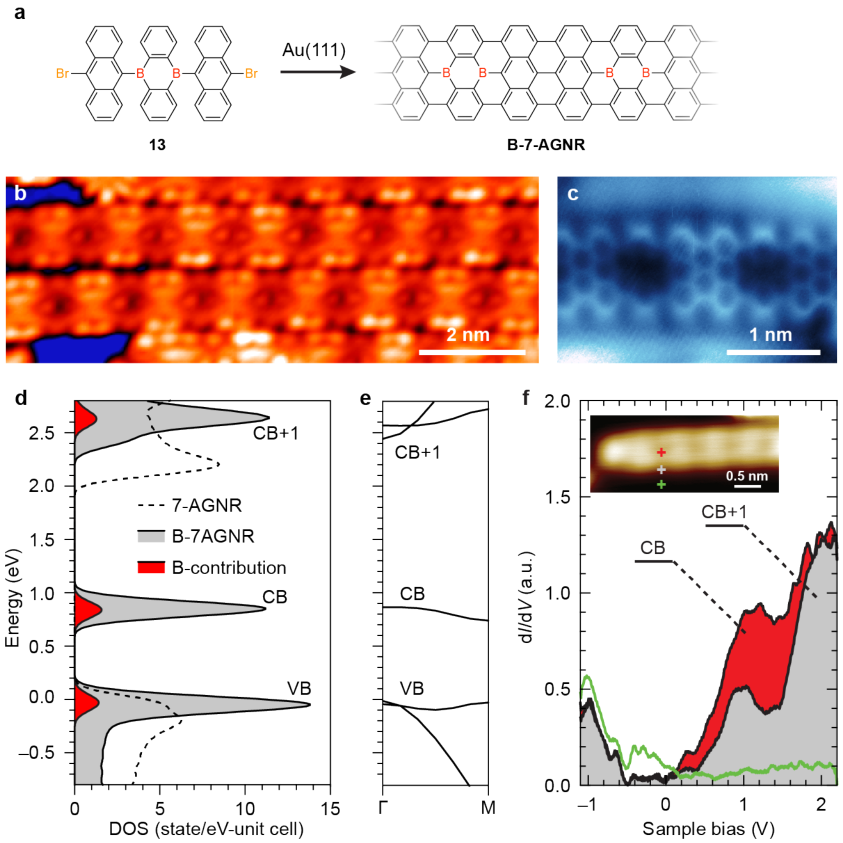

Figure 15. a) Schematic representation of the bottom-up synthesis of B-7-AGNRs on Au(111). b) STM topographic image of fully cyclized B-7-AGNRs. c) ncAFM image of B-7-AGNRs. The position of boron dopants appears darker in the frequency shift image as the empty p-orbital on B-atoms strongly interactions with the free valences of the underlying Au substrate. d) Calculated total DOS for B-7-AGNRs (gray) and the contribution from B-atoms to the DOS (red) using the *GW* approximation and including screening effects from Au(111) substrate. for comparison the DOS for undoped 7-AGNRs is plotted as a dotted line. VB maximum is set to 0 eV. e) Calculated quasiparticle band structure of B-7-AGNRs (using *GW* approximation). f) d*I*/d*V* spectrum of B-7-AGNRs recorded at the positions marked in the inset. While CB and CB+1 can clearly be identified in the spectrum the position of the VB coincides with the surface state of the Au(111) substrate. Reproduced with permission from ref. [51], Copyright (2015) American Chemical Society.

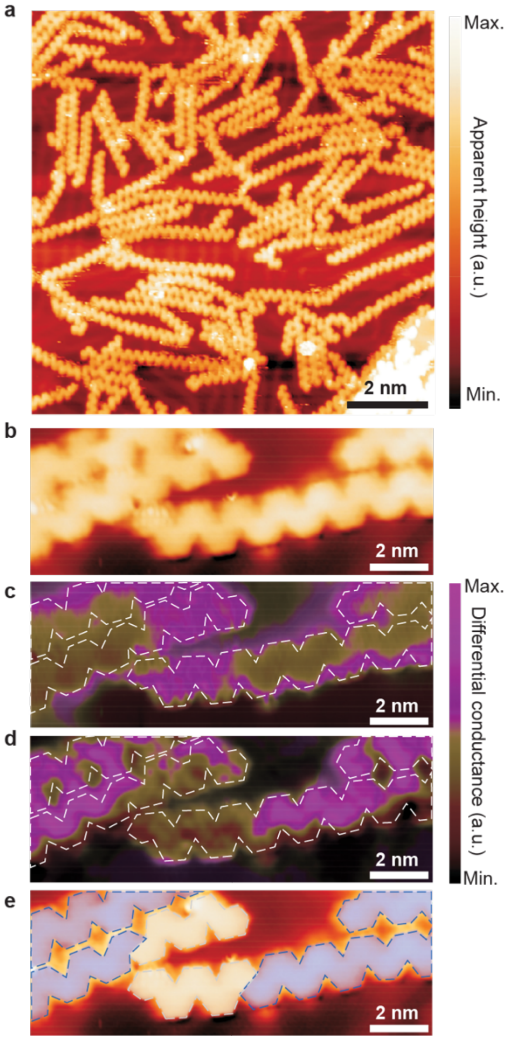

Figure 16. a) Large area STM image of segmented CGNRs formed by sequential co-deposition of **6** and **11**. b) STM topographic image of a **6**/**11** CGRN interface. c-d) d*I*/d*V* maps recorded at –0.35 V and –1.65 V, respectively. e) Overlay of topographic STM image illustrating the segmentation pattern in **6**/**11** CGRNs. Reproduced with permission from ref. [44], Copyright (2014) Nature Publishing Group.

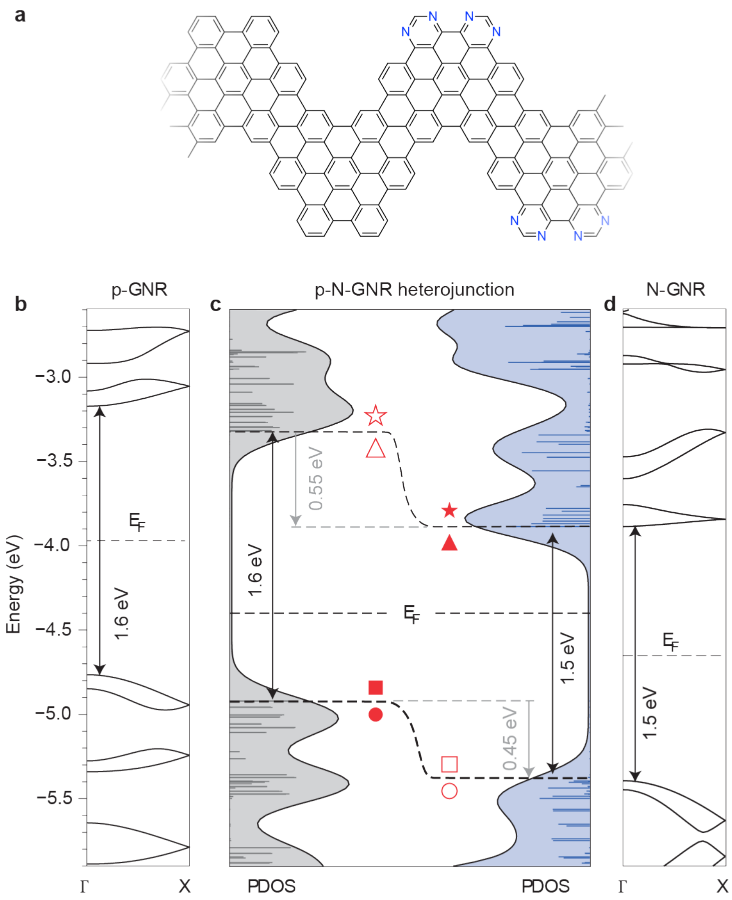

Figure 17. a) Schematic representation of the structure of a **6**/**11** CGNR heterojunction interface. b,d) DFT calculated band structure of pristine CGNRs (b) and nitrogen doped CGNR (d). c) PDOS of the p-GNR segment (left, grey) and the N-GNR segment (right, blue) of the heterojunction shown in a). The p-N-GNR heterojunction exhibits a staggered gap configuration with band offsets of 0.45 eV (VB) and 0.55 eV (CB). Reproduced with permission from ref. [44], Copyright (2014) Nature Publishing Group.

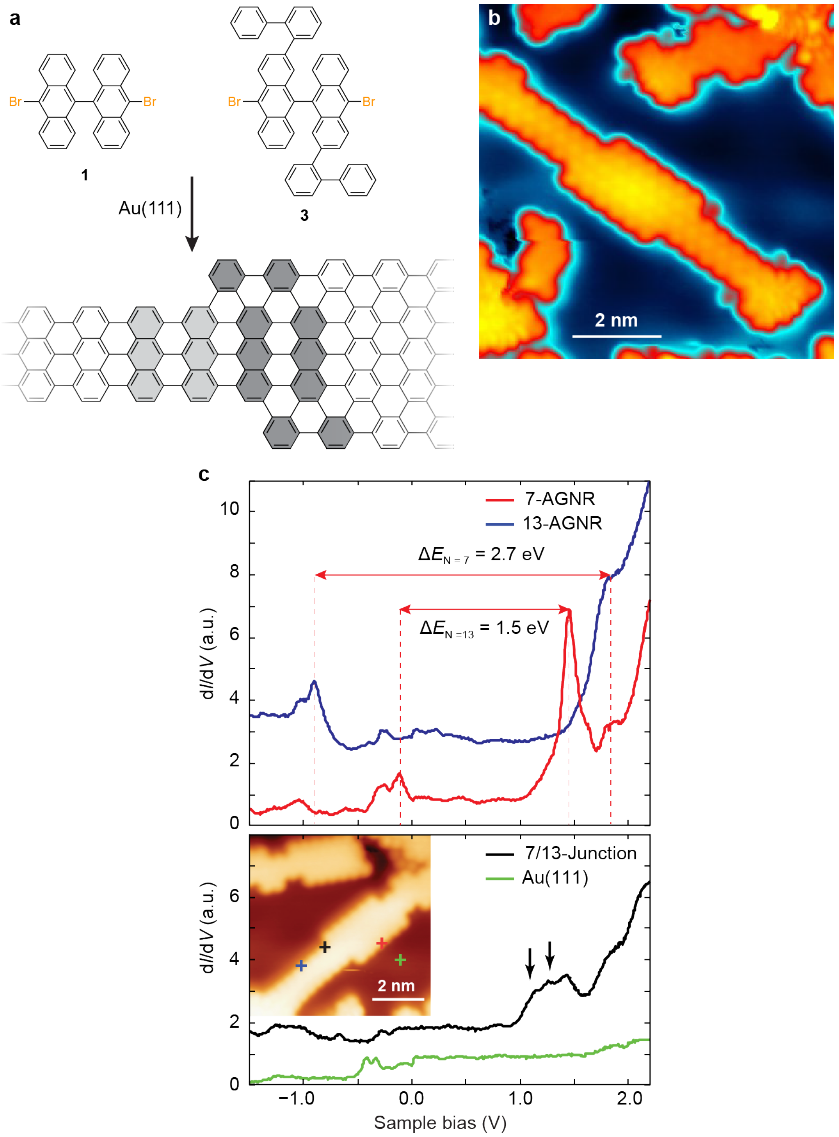

Figure 18. a) Synthesis of 7/13-AGNR heterojunctions from molecular building blocks **1** and **2**. b) STM topographic image of a 7/13-AGNR heterojunction. c) d*I*/d*V* spectroscopy of 7/13-AGNR heterojunction electronic structure recorded on a 7-ANGR segment (blue), a 13-AGNR segment (red), at the 7/13-AGNR heterojunction (black), and on the Au(111) surface. Reproduced with permission from ref. [54], Copyright (2015) Nature Publishing Group.

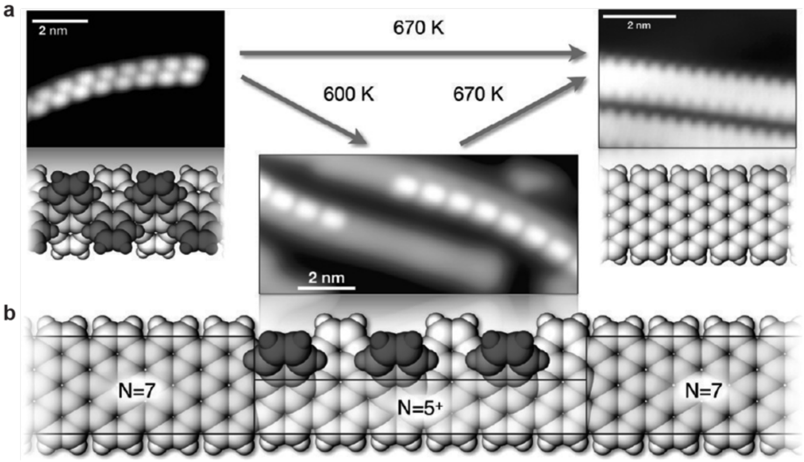

Figure 19. GNR heterojunctions by partial cyclodehydrogenation of polyanthrylene oligomers. (a) STM images and CPK models demonstrating the synthesis of AGNRs starting from *poly*-**1** on a Au(111) substrate. b) Annealing at a reduced temperature of 600 K results in partial cyclodehydrogenation and produces intraribbon 7/5^{+}/7-AGNR heterojunctions. Reproduced with permission from ref. [55], Copyright (2012) American Chemical Society.

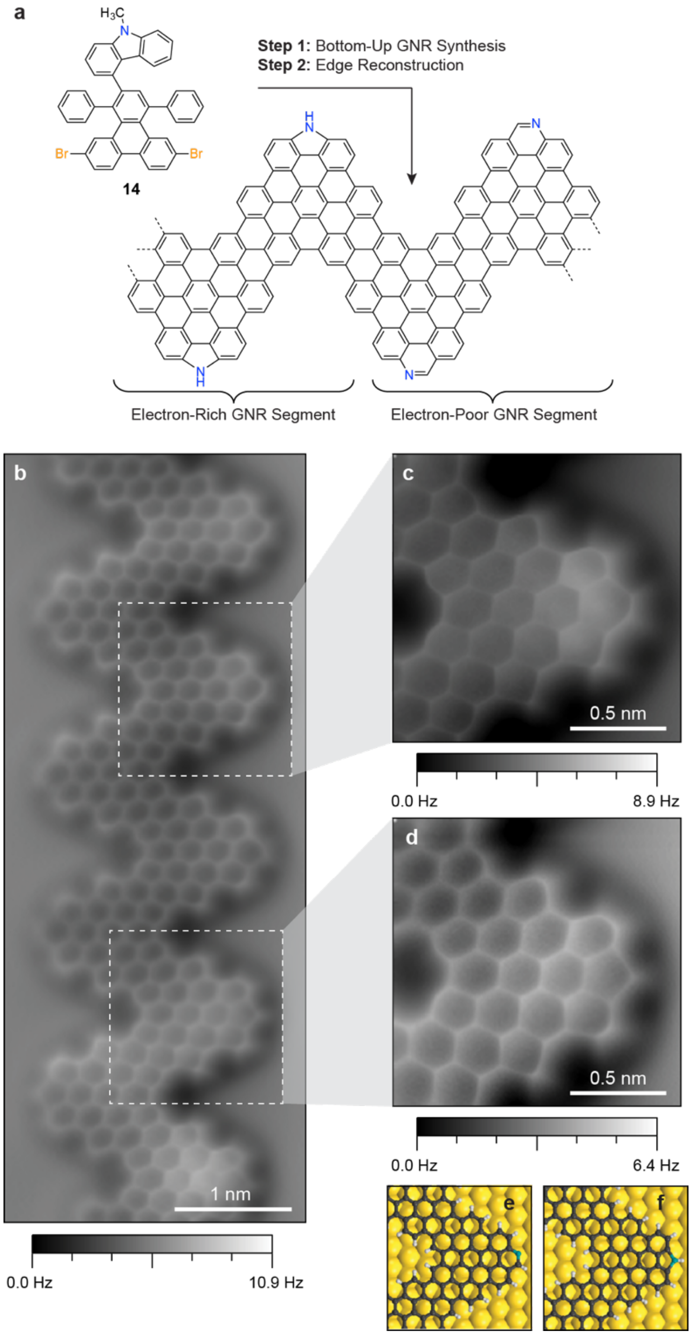

Figure 20. a) Schematic representation of the bottom-up synthesis of segmented nitrogen-doped CGNRs through edge reconstruction. Electron-rich carbazole and electron-poor phenanthridine subunits along the edges emerge from a thermal rearrangement of the 9-methyl-9*H*-carbazole in building block **1**. b) nc-AFM image CGNR heterostructure on Au(111) featuring discrete segments of fused phenanthridine and carbazole groups. c-d) nc-AFM image of phenanthridine and carbazole fused CGNR. e-f) Ball and stick model of phenanthridine and carbazole fused GNRs

serves as a guide to the eye. Reproduced with permission from ref. [56], Copyright (2016) John Wiley and Sons

5 References

1. Novoselov KS,Geim AK,Morozov SV,Jiang D,Zhang Y,Dubonos SV,Grigorieva IV,Firsov AA (2004) Science 306:666-669
2. Novoselov KS,Geim AK,Morozov SV,Jiang D,Katsnelson MI,Grigorieva IV,Dubonos SV,Firsov AA (2005) Nature 438:197-200
3. Geim AK,Novoselov KS (2007) Nat Mater 6:183-191
4. Castro Neto AH,Guinea F,Peres NMR,Novoselov KS,Geim AK (2009) Reviews of Modern Physics 81:109-162
5. Han MY,Ozyilmaz B,Zhang YB,Kim P (2007) Physical Review Letters 98
6. Zhang YB,Tan YW,Stormer HL,Kim P (2005) Nature 438:201-204
7. Stankovich S,Dikin DA,Dommett GHB,Kohlhaas KM,Zimney EJ,Stach EA,Piner RD,Nguyen ST,Ruoff RS (2006) Nature 442:282-286
8. Dikin DA,Stankovich S,Zimney EJ,Piner RD,Dommett GHB,Evmenenko G,Nguyen ST,Ruoff RS (2007) Nature 448:457-460
9. Kim KS,Zhao Y,Jang H,Lee SY,Kim JM,Kim KS,Ahn JH,Kim P,Choi JY,Hong BH (2009) Nature 457:706-710
10. Wang X,Zhi LJ,Müllen K (2008) Nano Lett 8:323-327
11. Schedin F,Geim AK,Morozov SV,Hill EW,Blake P,Katsnelson MI,Novoselov KS (2007) Nat Mater 6:652-655
12. Hill EW,Geim AK,Novoselov K,Schedin F,Blake P (2006) Ieee T Magn 42:2694-2696
13. Heersche HB,Jarillo-Herrero P,Oostinga JB,Vandersypen LMK,Morpurgo AF (2007) Nature 446:56-59
14. Geim AK (2009) Science 324:1530-1534
15. Tapaszto L,Dobrik G,Lambin P,Biro LP (2008) Nat Nanotechnol 3:397-401
16. Wang XR,Ouyang YJ,Li XL,Wang HL,Guo J,Dai HJ (2008) Physical Review Letters 100
17. Kosynkin DV,Higginbotham AL,Sinitskii A,Lomeda JR,Dimiev A,Price BK,Tour JM (2009) Nature 458:872-875
18. Tao CG,Jiao LY,Yazyev OV,Chen YC,Feng JJ,Zhang XW,Capaz RB,Tour JM,Zettl A,Louie SG,Dai HJ,Crommie MF (2011) Nat Phys 7:616-620
19. Li X,Wang X,Zhang L,Lee S,Dai H (2008) Science 319:1229-1232
20. Jiao LY,Zhang L,Wang XR,Diankov G,Dai HJ (2009) Nature 458:877-880
21. Xie LM,Wang HL,Jin CH,Wang XR,Jiao LY,Suenaga K,Dai HJ (2011) J Am Chem Soc 133:10394-10397
22. Cai J,Ruffieux P,Jaafar R,Bieri M,Braun T,Blankenburg S,Muoth M,Seitsonen AP,Saleh M,Feng X,Müllen K,Fasel R (2010) Nature 466:470-473
23. Lafferentz L,Ample F,Yu H,Hecht S,Joachim C,Grill L (2009) Science 323:1193-1197
24. Bombis C,Ample F,Lafferentz L,Yu H,Hecht S,Joachim C,Grill L (2009) Angew Chem Int

Edit 48:9966-9970

25. Lafferentz L,Eberhardt V,Dri C,Africh C,Comelli G,Esch F,Hecht S,Grill L (2012) Nat Chem 4:215-220

26. Björk J,Stafström S,Hanke F (2011) J Am Chem Soc 133:14884-14887

27. Linden S,Zhong D,Timmer A,Aghdassi N,Franke JH,Zhang H,Feng X,Müllen K,Fuchs H,Chi L,Zacharias H (2012) Physical Review Letters 108

28. Bjork J,Hanke F,Stafstrom S (2013) J Am Chem Soc 135:5768-5775

29. Bjork J (2016) J Phys-Condens Mat 28

30. Batra A,Cvetko D,Kladnik G,Adak O,Cardoso C,Ferretti A,Prezzi D,Molinari E,Morgante A,Venkataraman L (2014) Chem Sci 5:4419-4423

31. Simonov KA,Vinogradov NA,Vinogradov AS,Generalov AV,Zagrebina EM,Martensson N,Cafolla AA,Carpy T,Cunniffe JP,Preobrajenski AB (2015) J Phys Chem C 119:880-881

32. Bronner C,Bjork J,Tegeder P (2015) J Phys Chem C 119:486-493

33. Sun Q,Zhang C,Li ZW,Kong HH,Tan QG,Hu AG,Xu W (2013) J Am Chem Soc 135:8448-8451

34. Riss A,Wickenburg S,Gorman P,Tan LZ,Tsai H-Z,de Oteyza DG,Chen Y-C,Bradley AJ,Ugeda MM,Etkin G,Louie SG,Fischer FR,Crommie MF (2014) Nano Lett 14:2251-2255

35. Han P,Akagi K,Federici Canova F,Mutoh H,Shiraki S,Iwaya K,Weiss PS,Asao N,Hitosugi T (2014) Acs Nano 8:9181-9187

36. Han P,Akagi K,Canova FF,Mutoh H,Shiraki S,Iwaya K,Weiss PS,Asao N,Hitosugi T (2015) Acs Nano 9:3404-3405

37. Simonov KA,Vinogradov NA,Vinogradov AS,Generalov AV,Zagrebina EM,Martensson N,Cafolla AA,Carpy T,Cunniffe JP,Preobrajenski AB (2015) Acs Nano 9:3399-3403

38. Sánchez-Sánchez C,Dienel T,Deniz O,Ruffieux P,Berger R,Peng XL,Müllen K,Fasel R (2016) Acs Nano 10:8006-8011

39. Son Y-W,Cohen ML,Louie SG (2006) Physical Review Letters 97:216803

40. Yang L,Park C-H,Son Y-W,Cohen ML,Louie SG (2007) Physical Review Letters 99:186801

41. Chen Y-C,de Oteyza DG,Pedramrazi Z,Chen C,Fischer FR,Crommie MF (2013) ACS Nano 7:6123-6128

42. Zhang HM,Lin HP,Sun KW,Chen L,Zagranyarski Y,Aghdassi N,Duhm S,Li Q,Zhong DY,Li YY,Müllen K,Fuchs H,Chi LF (2015) J Am Chem Soc 137:4022-4025

43. Kimouche A,Ervasti MM,Drost R,Halonen S,Harju A,Joensuu PM,Sainio J,Liljeroth P (2015) Nat Commun 6:10177

44. Cai JM,Pignedoli CA,Talirz L,Ruffieux P,Sode H,Liang LB,Meunier V,Berger R,Li RJ,Feng XL,Müllen K,Fasel R (2014) Nat Nanotechnol 9:896-900

45. Bronner C,Stremlau S,Gille M,Brauße F,Haase A,Hecht S,Tegeder P (2013) Angewandte Chemie International Edition 52:4422-4425

46. Vo TH,Shekhirev M,Kunkel DA,Morton MD,Berglund E,Kong LM,Wilson PM,Dowben PA,Enders A,Sinitskii A (2014) Nat Commun 5:3189

47. Liu JZ,Li BW,Tan YZ,Giannakopoulos A,Sanchez-Sanchez C,Beljonne D,Ruffieux P,Fasel R,Feng XL,Müllen K (2015) J Am Chem Soc 137:6097-6103

48. Ruffieux P,Wang SY,Yang B,Sanchez-Sanchez C,Liu J,Dienel T,Talirz L,Shinde P,Pignedoli CA,Passerone D,Dumslaff T,Feng XL,Müllen K,Fasel R (2016) Nature 531:489-492

49. Vo TH,Perera UGE,Shekhirev M,Mehdi Pour M,Kunkel DA,Lu H,Gruverman A,Sutter E,Cotlet M,Nykypanchuk D,Zahl P,Enders A,Sinitskii A,Sutter P (2015) Nano Lett 15:5770-5777

50. Nguyen GD,Tom FM,Cao T,Pedramrazi Z,Chen C,Rizzo DJ,Joshi T,Bronner C,Chen YC,Favaro M,Louie SG,Fischer FR,Crommie MF (2016) J Phys Chem C 120:2684-2687

51. Cloke RR,Marangoni T,Nguyen GD,Joshi T,Rizzo DJ,Bronner C,Cao T,Louie SG,Crommie MF,Fischer FR (2015) J Am Chem Soc 137:8872-8875

52. Kawai S,Saito S,Osumi S,Yamaguchi S,Foster AS,Spijker P,Meyer E (2015) Nat Commun 6:8098

53. Cai J,Pignedoli CA,Talirz L,Ruffieux P,Söde H,Liang L,Meunier V,Berger R,Li R,Feng X,Müllen K,Fasel R (2014) Nat Nano 9:896-900

54. Chen Y-C,Cao T,Chen C,Pedramrazi Z,Haberer D,de OteyzaDimas G,Fischer FR,Louie SG,Crommie MF (2015) Nat Nano 10:156-160

55. Blankenburg S,Cai J,Ruffieux P,Jaafar R,Passerone D,Feng X,Müllen K,Fasel R,Pignedoli CA (2012) ACS Nano 6:2020-2025

56. Marangoni T,Haberer D,Rizzo DJ,Cloke RR,Fischer FR (2016) Chemistry European Journal ASAP:DOI: 10.1002/chem.201603497

57. Cano-Marquez AG,Rodriguez-Macias FJ,Campos-Delgado J,Espinosa-Gonzalez CG,Tristan-Lopez F,Ramirez-Gonzalez D,Cullen DA,Smith DJ,Terrones M,Vega-Cantu YI (2009) Nano Lett 9:1527-1533

58. Elias AL,Botello-Mendez AR,Meneses-Rodriguez D,Gonzalez VJ,Ramirez-Gonzalez D,Ci L,Munoz-Sandoval E,Ajayan PM,Terrones H,Terrones M (2010) Nano Lett 10:366-372

59. Ma L,Wang J,Ding F (2013) ChemPhysChem 14:47-54